



Glucose-assisted synthesis of $\text{Na}_3\text{V}_2(\text{PO}_4)_3/\text{C}$ composite as an electrode material for high-performance sodium-ion batteries



Guangqiang Li, Danlu Jiang, Hui Wang, Xinzheng Lan, Honghai Zhong, Yang Jiang*

School of Materials Science and Engineering, Hefei University of Technology, Hefei, Anhui 230009, PR China

HIGHLIGHTS

- $\text{Na}_3\text{V}_2(\text{PO}_4)_3/\text{C}$ was synthesised through glucose-assisted carbon-thermal reduction.
- $\text{Na}_3\text{V}_2(\text{PO}_4)_3/\text{C}$ has 3.4 V voltage plateau against Na with ca. 98 mAh g⁻¹.
- The product exhibited excellent cycling stability and rate performance.
- The $\text{Na}_3\text{V}_2(\text{PO}_4)_3/\text{C}$ can be used as both a cathodic and an anodic material.
- The structure changes of $\text{Na}_3\text{V}_2(\text{PO}_4)_3$ during electrode reactions were simulated.

ARTICLE INFO

Article history:

Received 13 February 2014

Received in revised form

29 March 2014

Accepted 13 April 2014

Available online 9 May 2014

Keywords:

Sodium-ion batteries

$\text{Na}_3\text{V}_2(\text{PO}_4)_3/\text{C}$

Cathode and anode materials

NASICON-structured compounds

Carbon-thermal reduction

ABSTRACT

A novel electrode material for sodium-ion batteries (NIBs), $\text{Na}_3\text{V}_2(\text{PO}_4)_3$ with a rhombohedral, Na⁺ superionic conductor (NASICON)-type structure, was synthesised via a solid-state carbon-thermal reduction reaction assisted by mechanochemical activation. Electron microscopy analysis showed that the synthesised $\text{Na}_3\text{V}_2(\text{PO}_4)_3$ particles had an average size of 300 nm, being coated with a uniform layer of carbon 3 nm in thickness. As a cathode material, $\text{Na}_3\text{V}_2(\text{PO}_4)_3/\text{C}$ exhibited an initial specific discharge capacity of 98.17 mAh g⁻¹ at 0.1C for potentials ranging from 2.5 to 3.8 V. This was owing to the V³⁺/V⁴⁺ redox couple, which corresponded to the two-phase transition between $\text{Na}_3\text{V}_2(\text{PO}_4)_3$ and $\text{NaV}_2(\text{PO}_4)_3$. The cathode lost 4.92% of its discharge specific capacity after 50 cycles. As an anode material, $\text{Na}_3\text{V}_2(\text{PO}_4)_3/\text{C}$ exhibited an initial specific discharge capacity of 63.2 mAh g⁻¹ at 0.1C for potentials ranging from 1.0 to 2.5 V. This was owing to the V²⁺/V³⁺ redox couple, which corresponded to the two-phase transition between $\text{Na}_3\text{V}_2(\text{PO}_4)_3$ and $\text{Na}_4\text{V}_2(\text{PO}_4)_3$. The anode lost approximately 5.41% of its discharge specific capacity after 50 cycles. The three-dimensional channel structure of $\text{NaV}_2(\text{PO}_4)_3$ and the changes induced in its lattice parameters during the charge/discharge processes were simulated on the basis of density functional theory.

© 2014 Elsevier B.V. All rights reserved.

1. Introduction

Since the combustion of fossil fuels results in air pollution and increases the greenhouse effect, much attention is being focused on the exploitation of new energy sources, such as solar, wind, tidal, and geothermal ones [1]. Significant progress has been made in the development of renewable energy technologies. The development of devices and technologies for storing electrical energy is also important, as these will allow for hybrid electric vehicles (HEVs) and electric vehicles (EVs) and can act as back-ups for wind and solar energy sources [2–4]. Lithium-ion batteries (LIBs) are

considered the most efficient energy storage systems and are used widely in portable electronic devices, owing to their high open-circuit voltage, high energy density, flexibility and lightweight design, long cycle life, and environmental friendliness [5,6]. However, lithium is not available in the amounts necessary for meeting the increasing market demand. Thus, rechargeable batteries based on alternative, abundantly available materials need to be developed [7].

Sodium-ion batteries (NIBs) are a promising alternative to LIBs for large-scale energy storage applications, because of the high availability of sodium, its low cost, and the similarity in the intercalation chemistry of sodium and lithium [8–10]. The fully developed lithium electrochemical system can be exploited for developing the Na counterpart [11]. A number of studies have focused on developing improved electrode materials for NIBs in the

* Corresponding author. Tel./fax: +86 551 62904358.

E-mail address: apjiang@hfut.edu.cn (Y. Jiang).

last few years. For example, electrode materials such as $\text{Na}_2\text{V}_6\text{O}_{16}$ [12], $\text{NaV}_6\text{O}_{15}$ [13], $\text{Na}_{0.6}\text{VO}_2$ [14], Na_xVO_2 [15–17], $\text{Na}_{0.71}\text{CoO}_2$ [18], $\text{Na}_{0.44}\text{MnO}_2$ [19,20], $\text{Na}_x[\text{Ni}_{1/3}\text{Mn}_{2/3}]\text{O}_2$ [21], $\text{Na}[\text{Ni}_{1/3}\text{Fe}_{1/3}\text{Mn}_{1/3}]\text{O}_2$ [22], $\text{Na}_3\text{Cr}_2(\text{PO}_4)_3$ [23], $\text{Na}_2\text{MnP}_2\text{O}_7$ [24], $\text{Na}_2\text{CoP}_2\text{O}_7$ [25,26], $\text{Na}_4\text{Co}_3(\text{PO}_4)_2\text{P}_2\text{O}_7$ [27], $\text{Na}_2\text{MnPO}_4\text{F}$ [28], $\text{Na}_2\text{FePO}_4\text{F}$ [29], $\text{Na}_3\text{M}_2(\text{PO}_4)_2\text{F}_3$ [30], $\text{Na}_3\text{V}_2(\text{PO}_4)_2\text{F}_3$ [11,31], $\text{Na}_2\text{Ti}_3\text{O}_7$ [32–35], $\text{Li}_4\text{Ti}_5\text{O}_{12}$ [36], and $\text{Na}_2\text{C}_8\text{H}_4\text{O}_4$ [37] have been explored for use as active electrode materials in NIBs.

To further improve the energy density, safety, and life cycle of NIBs [38], new cathodic materials need be developed. Owing to their high redox voltage and steady reversibility, polyanionic materials have attracted a great deal of interest as cathodic materials for NIBs. Of late, Na^+ superionic conductor (NASICON)-type insertion hosts are being investigated as prospective electrode materials for NIBs. These materials have the following general molecular formula: $\text{A}_x\text{M}_2(\text{XO}_4)_3$, where $\text{A} = \text{Na}$ or Li ; $\text{M} = \text{Ti}$, V , or Fe ; and $\text{X} = \text{P}$, S , Mo , W , or As . In the crystal structure of these materials, which have a NASICON framework, the MO_6 octahedral units share all their corners with XO_4 tetrahedra, and the XO_4 tetrahedral units share all three corners with MO_6 octahedra. This allows for the formation of interstitial and conduction channels along the c -axis direction; alkali metal ions (Na^+ or Li^+) can occupy the interstitial positions in these channels [39]. The energies of the $\text{M}^{(m+1)+}/\text{M}^{m+}$ redox couples are strongly influenced by the counteraction in the polyanion tetrahedron (XO_4). In particular, phosphate-based Na-insertion hosts have attracted significant interest, because of the strong $\text{P}-\text{O}$ bond in the $(\text{PO}_4)^{3-}$ units; the bond provides structural stability even in the high-charge states and lowers the energy of the top of the $\text{O}-2p$ bands. Hence, the cathodic material has a higher intrinsic voltage limit, which is determined by the pinning of the Fermi energy at the top of the $\text{O}-2p$ bands [40].

Rhombohedral $\text{Na}_3\text{V}_2(\text{PO}_4)_3$ (NVP), which is a polyanionic material, has a robust structure, good ionic mobility, a high theoretical specific capacity (117.6 mAh g^{-1}), and a high operating voltage (up to 3.4 V). As a result, it should be a suitable cathodic material for NIBs. NVP consists of a three-dimensional (3D) framework of VO_6 octahedra and PO_4 tetrahedra, which share oxygen vertices, hosting Na ions in the relatively large interstitial sites. However, the poor intrinsic electronic conductivity of NVP, which results from the separation of the VO_6 octahedra from the PO_4 tetrahedra in the rhombohedral structure, limits its practical use. Recently, Jian et al. [41] reported a sugar-assisted one-step solid-state reaction to prepare NVP/C powders with an average particle size of $3 \mu\text{m}$. These powders exhibited an initial discharge capacity of 93.0 mAh g^{-1} at a current rate of 0.05C; however their rate capabilities and cycling performance were not high enough. Lim et al. [42] synthesised NVP by a polyvinylpyrrolidone (PVP)-assisted sol–gel method; the fabricated sample exhibited a discharge capacity of 84.8 mAh g^{-1} . Further, Jung and Lim [43] employed a sol–gel method to synthesise graphene-coated NVP, which exhibited a slightly low discharge capacity. In view of these previous reports, finding a simple, low-cost, and efficient synthesis process is one of the main concerns related to the use of such materials in NIBs.

In this study, we employed a simple solid-state reaction-based method to synthesise NVP-based cathodic materials using low-cost glucose as the carbon source. Glucose was used because it could be readily dispersed in the precursor, owing to its small molecular size and chain structure. As result, carbon was generated *in situ* from the glucose, which was distributed uniformly in the entire reaction system, resulting in improved electrochemical performance. The charge–discharge capacities and cycling performances of the cathodic materials when used in NIBs were investigated. In addition, the diffusion coefficient of Na ions in NVP was determined through cyclic voltammetry (CV) and electrochemical impedance spectroscopy (EIS). Finally, we performed structure–energy

calculations on the basis of density functional theory (DFT) to elucidate the Na^+ extraction/insertion mechanism in the NVP structure during cycling.

2. Experimental

2.1. Synthesis

The NVP/C powders were synthesised by a carbon-thermal reduction method. NH_4VO_3 and $\text{NaH}_2\text{PO}_4 \cdot 2\text{H}_2\text{O}$ were used as the starting materials and glucose (in the appropriate amount) was used as the carbon source. The materials were mixed and dispersed in alcohol and then ball milled for 24 h in a planetary mill. Then, the obtained mixture was dried at 80°C in an oven to evaporate the alcohol. After the alcohol had been evaporated, the remaining precursor was transferred into a porcelain boat and calcined at the required temperature for 4 h under an Ar flow in a tube furnace. This yielded the NVP/C composite.

2.2. Material characterisation

The phases and crystal structures of the synthesised materials were analysed using a powder X-ray diffraction (XRD) analysis system (D/MAX2500V, Rigaku, Japan) equipped with a Cu $K\alpha$ radiation source. The morphological features of the powder particles were analysed by field-emission scanning electron microscopy (FESEM)(SU8020, Hitachi, Japan) and high-resolution field-emission transmission electron microscopy (HRTEM)(JEM-2100F, JEOL, Japan).

2.3. Electrochemical performance tests

The cathodes used for the electrochemical tests consisted of 75 wt% active material (i.e., the NVP/C composite), 15 wt% acetylene black, and 10 wt% polyvinylidene fluoride (PVDF), which was used as the binder. A slurry of the mixture was prepared by adding an appropriate amount of *N*-methyl-2-pyrrolidone (NMP) to it. This slurry was cast on an aluminium foil using a doctor's blade. The slurry was then dried at 120°C for 12 h in a vacuum oven. Electrodes of the desired size were then punched out from the dried slurry. Electrochemical cells based on the electrodes were assembled in a glove box filled with high-purity argon; pure sodium foil was used as the counter electrode, 1 M NaClO_4 in propylene carbonate (PC) was used as the electrolyte, and glass fibre was used as the separator. The charge–discharge measurements were performed over potentials ranging from 2.5 V to 3.8 V and 1.0 V to 2.5 V (vs. Na^+/Na) at various C rates at room temperature. For the galvanostatic charge/discharge tests, the current rate was C/10 (11.76 mA g^{-1}) for both the charge and the discharge stages. We determined that a current rate of 1C corresponds to 117.6 mA g^{-1} on the basis of the theoretical capacity of the two-phase transition between $\text{Na}_3\text{V}_2(\text{PO}_4)_3$ and $\text{NaV}_2(\text{PO}_4)_3$ (117.6 mAh g^{-1}). For the rate-performance tests, all the electrochemical cells were charged to 3.8 V at a rate of C/10, and then discharged to 2.5 V at various C rates. Unless otherwise noted, all voltage values were referenced to the standard redox potential of Na^+/Na . CV measurements were performed using a CHI660D (Shanghai, China) electrochemical workstation at a scan rate of 0.05 mV s^{-1} over potentials ranging from 1.2 to 3.8 V (vs. Na^+/Na). EIS was performed using a three-electrode cell in which sodium foil was used as both the counter and the reference electrodes. EIS measurements were also performed using the above-mentioned electrochemical workstation over frequencies ranging from 100 kHz to 0.01 Hz during the discharge stage (2.5 V) by applying an AC signal of 5 mV.

3. Results and discussion

3.1. Structures and morphologies of the synthesised materials

The XRD patterns of the samples synthesised by carbon-thermal reduction at different sintering temperatures are shown in Fig. 1. The sample synthesised at 600 °C (Fig. 1(c)) exhibited amorphous characteristics. On the other hand, the diffraction peaks of the samples synthesised at 650 °C (Fig. 1(b)) and 900 °C (Fig. 1(a)) were suggestive of a pure NASICON-type $\text{Na}_3\text{V}_2(\text{PO}_4)_3$ structure that was free of impurities, indicating the completion of the reduction reaction. These results were in good agreement with those reported previously [41–43]. Thus, it was found that the phase-pure $\text{Na}_3\text{V}_2(\text{PO}_4)_3$ can be obtained by sintering at temperatures in the range of 650–900 °C. The sample prepared by sintering at 900 °C for 4 h, in order to restrain grain growth, had highly crystalline characteristics. The diffraction peaks of the samples could be attributed to a pure $\text{Na}_3\text{V}_2(\text{PO}_4)_3$ phase with a NASICON-type structure with the R-3c space group (167). This suggests that the presence of carbon did not affect the structure of $\text{Na}_3\text{V}_2(\text{PO}_4)_3$. The results of structural refinement showed that lattice parameters of the particles of the synthesised NVP powders were $a = 8.7212$ Å and $c = 21.8372$ Å; these values are consistent with those reported in the literature for $\text{Na}_3\text{V}_2(\text{PO}_4)_3$ [8,44]. Further, as can be seen from Fig. 1(a) and (b), no diffraction peaks related to carbon were noticed in the XRD patterns. This indicated that the residual carbon from the glucose was present in the composites in a very small amount and in an amorphous state. Finally, field-emission transmission electron microscopy (FETEM) images confirmed that the NVP nanoparticles were uniformly coated with carbon.

Fig. 2(a) shows the NASICON-type structure of $\text{Na}_3\text{V}_2(\text{PO}_4)_3$ projected on the (3 0 0) plane. The structure consists of a 3D open framework consisting of 3D channels; Na ions can easily migrate through these 3D channels. This results in extremely high ionic mobility. Each primitive cell of $\text{Na}_3\text{V}_2(\text{PO}_4)_3$ contains six $\text{Na}_3\text{V}_2(\text{PO}_4)_3$ formula units [41]. As illustrated in Fig. 2(a), each VO_6 octahedron shares corners with three PO_4 tetrahedrons. This builds up the framework anion $[\text{V}_2(\text{PO}_4)_3]^{3-}$ units along the c -axis, and each $[\text{V}_2(\text{PO}_4)_3]^{3-}$ unit is interlinked to the same neighbouring units by the PO_4 tetrahedron along the a -axis, forming the open 3D framework structure [8,41,42]. This arrangement leads to the formation of well-defined ion channels, with Na ions being located in the tunnel sites. These channels in the structure act as pathways for the diffusion of Na ions. Since it is open 3D structure, the special plane (300) was chosen to show how the sodium ions diffuse and there exists similar pathways in other planes, thus leading to the formation of 3D ions channels in this material. The diffusion of Na2

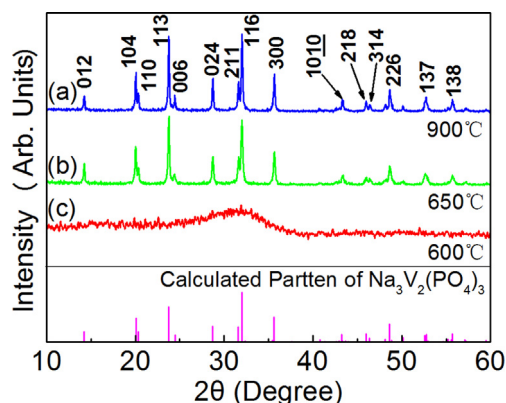


Fig. 1. Powder XRD patterns for the carbon-coated $\text{Na}_3\text{V}_2(\text{PO}_4)_3$ samples synthesised at (a) 900 °C, (b) 650 °C, and (c) 600 °C.

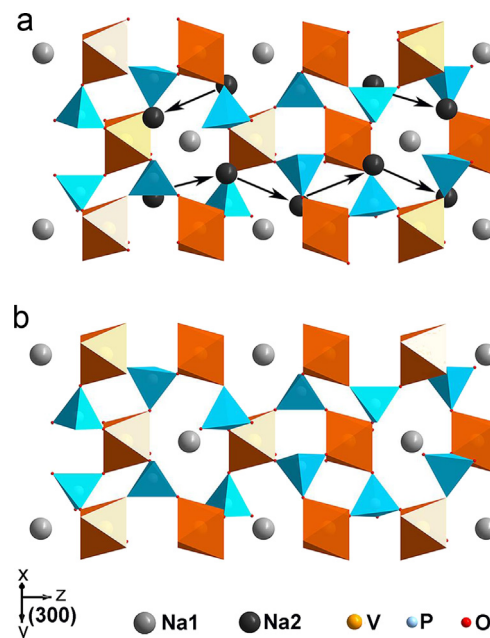


Fig. 2. Crystal structure, projected on the (3 0 0) plane, of (a) the synthesised $\text{Na}_3\text{V}_2(\text{PO}_4)_3$ sample before it was charged and (b) that of $\text{NaV}_2(\text{PO}_4)_3$ after all the Na^+ ions located at the Na2 sites had been extracted during the charging process. The arrows show the ions diffusion channels in (3 0 0) plane.

ions along a curved pathway is also indicated in Fig. 2. $\text{Na}_3\text{V}_2(\text{PO}_4)_3$ contains two kinds of Na sites, namely, M1 and M2 sites. Na ions selectively occupy the M1 (octahedral sites) and M2 (tetrahedral sites) sites [41]. Na1 ions occupy M1 sites and Na2 ions occupy M2 sites as shown in Fig. 2. The two independent Na atoms are located in the channels of the framework having two different oxygen environments. The M1 sites are situated between two adjacent $[\text{V}_2(\text{PO}_4)_3]^{3-}$ units along the c -axis, while the M2 sites are located at the same z value as the phosphorous atoms [8,42]. In the case all the M1 and M2 sites are occupied, a total of four Na ions are contained within each formula unit of $\text{Na}_4\text{V}_2(\text{PO}_4)_3$, with one Na ion being present at the M1 site and three at the M2 site [42]. However, recent studies have reported that Na ions occupy all the M1 sites and two-thirds of the M2 sites in the crystal structure of $\text{Na}_3\text{V}_2(\text{PO}_4)_3$ [41,42]. In fact, $\text{Na}_3\text{V}_2(\text{PO}_4)_3$ is more likely to be synthesised that is $\text{Na}_4\text{V}_2(\text{PO}_4)_3$, owing to the oxidation state of V^{3+} in $\text{Na}_3\text{V}_2(\text{PO}_4)_3$ being more stable than that of V^{2+} in $\text{Na}_4\text{V}_2(\text{PO}_4)_3$ [42].

In order to further investigate the crystal structure of NVP, first-principles calculations based on density functional theory (DFT) were performed using a plane-wave expansion of the wave function. The local-density approximation (LDA) + U and Broyden–Fletcher–Goldfarb–Shanno (BFGS) geometry optimisation methods were used to describe the crystal structure of $\text{NaV}_2(\text{PO}_4)_3$, as they would allow one to understand the Na^+ extraction/insertion mechanism and evaluate the stability of the synthesised materials during electrochemical reactions. The norm-conserving pseudo-potential was used for the electron–ion interactions, and the cut-off energy was set to 330 eV. The Brillouin zone sampling k -point set-mesh parameters were $3 \times 3 \times 2$. In order to reflect the stronger inductive effect in $\text{Na}_3\text{V}_2(\text{PO}_4)_3$, a higher U parameter of 4.2 eV was used [42]. The lattice parameters from our XRD measurements were used as the initial values for the calculation, and the calculation was performed for 150 iterations, that is, until the results were almost constant. After all the Na^+ ions located at the M2 sites had been extracted during the charging process, the compound underwent a phase transformation to $\text{NaV}_2(\text{PO}_4)_3$, which also had a NASICON-type structure. A projection of this structure on the (3

Table 1Lattice parameters of $\text{Na}_3\text{V}_2(\text{PO}_4)_3$, $\text{NaV}_2(\text{PO}_4)_3$ and $\text{Na}_4\text{V}_2(\text{PO}_4)_3$.

	<i>a</i> (Å)	<i>c</i> (Å)	Volume (Å ³)
$\text{Na}_3\text{V}_2(\text{PO}_4)_3$	8.7200	21.764	1433.19
$\text{NaV}_2(\text{PO}_4)_3$	8.4326	21.0205	1294.82
$\text{Na}_4\text{V}_2(\text{PO}_4)_3$	8.9361	21.2876	1472.16

0 0) plane is shown in Fig. 2(b). According to the results of the calculation, the lattice parameters of $\text{NaV}_2(\text{PO}_4)_3$ corresponded to the *R*-3*c* space group (167) and were $a = 8.3738$ Å and $c = 21.4261$ Å; these values are very similar to those of $\text{Na}_3\text{V}_2(\text{PO}_4)_3$ [45]. The lattice parameters and other structural information, including the atomic positions of $\text{Na}_3\text{V}_2(\text{PO}_4)_3$, $\text{NaV}_2(\text{PO}_4)_3$ and $\text{Na}_4\text{V}_2(\text{PO}_4)_3$, are listed in Tables 1–4. The results indicate that the 3D framework of NVP is not damaged during the charging and discharging processes and that the volumetric change is 9.65%. This suggests that the fact the change in volume is small might facilitate the diffusion of Na ions in the structure and cause minimal distortion of the crystal lattice. Thus, using the synthesised NVP/C powders with a stable NASICON-type structure as an electrode material for NIBs should result in superior charge–discharge rate performance.

The morphological features of the synthesised NVP/C powders are shown in Fig. 3. The low-magnification FESEM image of the NVP/C sample synthesised at 900 °C (Fig. 3(a)) shows that its particles, whose average size was 1.0 µm, had an irregular morphology. High-magnification images of the sample (Fig. 3(b)) showed that its primary particles were less than 300 nm in size and agglomerated to form larger secondary particles with sizes on the micrometer scale. This is to be expected in the case of products formed through solid-state reactions that occur at high temperatures and last for several hours. The smaller primary particles, which have a larger specific surface area, allow for the ready transfer of Na ions and electrons during the cycling process. This likely results in better electrochemical performance than that when larger particles with lower specific surface areas are used. Moreover, a high surface area increases the electrode/electrolyte contact area and promotes greater ion diffusion between the cathode and the electrolyte during the electrochemical reaction, resulting in high rate performance [46].

The HRTEM image in Fig. 3(c) shows clearly that the NVP powder particles were dispersed well in the carbon matrix and were several hundreds of nanometres in size. Further, it can be seen clearly from Fig. 3(d) that the particles were uniformly coated with a layer of amorphous carbon and that this coating was approximately 3 nm in thickness. No lattice fringes related to the surface carbon layer were observed; this was proof of its amorphous nature. The content of residual carbon was measured to be 2.9 wt% from gravimetric analysis after dissolution of the material in a hydrochloric solution. In this study, glucose not only acts as a reductant, reducing V^{5+} to V^{3+} during the heat-treatment process, but also results in the formation of network consisting of carbon shell layers. This network enhances the electronic contact between the

Table 2Atomic positions of the constituent elements in $\text{Na}_3\text{V}_2(\text{PO}_4)_3$. These values, which were taken from our XRD results, were used as the initial values for the CASTEP-based simulation of $\text{NaV}_2(\text{PO}_4)_3$.

	<i>x</i>	<i>y</i>	<i>z</i>
V1	0.3333	0.6667	0.01952
Na1	0.3333	0.6667	0.1667
Na2	0.6667	0.9664	0.0833
P1	−0.03999	0.3333	0.0833
O1	0.14318	0.49754	0.07959
O2	0.54553	0.85044	−0.02623

Table 3Atomic positions of the constituent elements in $\text{NaV}_2(\text{PO}_4)_3$ obtained from calculations.

	<i>x</i>	<i>y</i>	<i>z</i>
V1	0.3333	0.6667	0.02250
Na1	0.3333	0.6667	0.1667
P1	−0.04790	0.3333	0.0833
O1	0.14060	0.50240	0.07780
O2	0.52830	0.83780	−0.02600

particles. It also restricts the growth of the NVP crystalline particles and prevents them from agglomerating during the annealing process. This further improves the electrochemical properties of the synthesised material. Fig. 3(e) and (f) also shows that the NVP/C composite was highly crystalline and exhibited clear lattice fringes. It is believed that materials with higher crystallinity undergo minimal crystal lattice distortion and form smoother ion-migration channels. In the case of the NVP/C composite, these channels facilitate the diffusion of Na ions within the structure. The clear lattice fringes with interfringe distances of 0.253 and 0.282 nm (see Fig. 3(f)) were in keeping with the *d*-spacings of the (3 0 0) and (1 1 6) planes of NASICON-type NVP, respectively. This was also true for the selected area electron diffraction (SAED) patterns shown in the figure. These results further confirmed that the synthesised powder with sub-micron size particles was crystalline in nature.

3.2. Electrochemical performance

Fig. 4(a) shows the CV curves corresponding to the first two cycles of the NVP/C composite for potentials ranging from 1.2 to 3.8 V (vs. Na^+/Na); the scan rate was 0.05 mV s^{−1}. It can be seen clearly that the electrode made from the NASICON-type material displayed two pairs of well-defined redox peaks between 1.2 and 3.8 V. Thus, the material exhibited outstanding reversibility with respect to the Na extraction/insertion reactions. The oxidation (Na extraction) and reduction (Na insertion) peaks located at 3.51 and 3.30 V (vs. Na^+/Na), respectively, that is, the peaks in the high-voltage region correspond to the extraction/insertion of two Na ions located at the M2 sites into a single formula unit of the compound. These peaks can be assigned to the $\text{V}^{4+}/\text{V}^{3+}$ redox couple on the basis of the two-phase transition between $\text{Na}_3\text{V}_2(\text{PO}_4)_3$ and $\text{NaV}_2(\text{PO}_4)_3$. In the low-voltage range, the redox peaks located at 1.71 and 1.58 V could be attributed to the $\text{V}^{3+}/\text{V}^{2+}$ redox couple, which corresponds to the compositional transition between $\text{Na}_3\text{V}_2(\text{PO}_4)_3$ and $\text{Na}_4\text{V}_2(\text{PO}_4)_3$. The polarisation voltage was approximately 0.2 V for the $\text{V}^{4+}/\text{V}^{3+}$ redox couple and 0.1 V for the $\text{V}^{3+}/\text{V}^{2+}$ redox couple. It is known that well-defined oxidation and reduction peaks as well as small differences in the polarisation voltages corresponding to the peaks, which depend on the transitions between the $\text{V}^{3+}/\text{V}^{4+}$ and $\text{V}^{2+}/\text{V}^{3+}$ redox states, are indicative of high reversibility with respect to the carbon-assisted extract/insertion of Na ions. Therefore, the synthesised NVP/C composite should exhibit excellent charge–discharge performance as an electrode material.

Table 4Atomic positions of the constituent elements in $\text{Na}_4\text{V}_2(\text{PO}_4)_3$ obtained from calculations.

	<i>x</i>	<i>y</i>	<i>z</i>
V1	0.3333	0.6667	0.02075
Na1	0.3333	0.6667	0.1667
Na2	0.6667	0.96801	0.0833
P1	−0.03624	0.3333	0.0833
O1	0.14383	0.49351	0.08319
O2	0.54055	0.86346	−0.02482

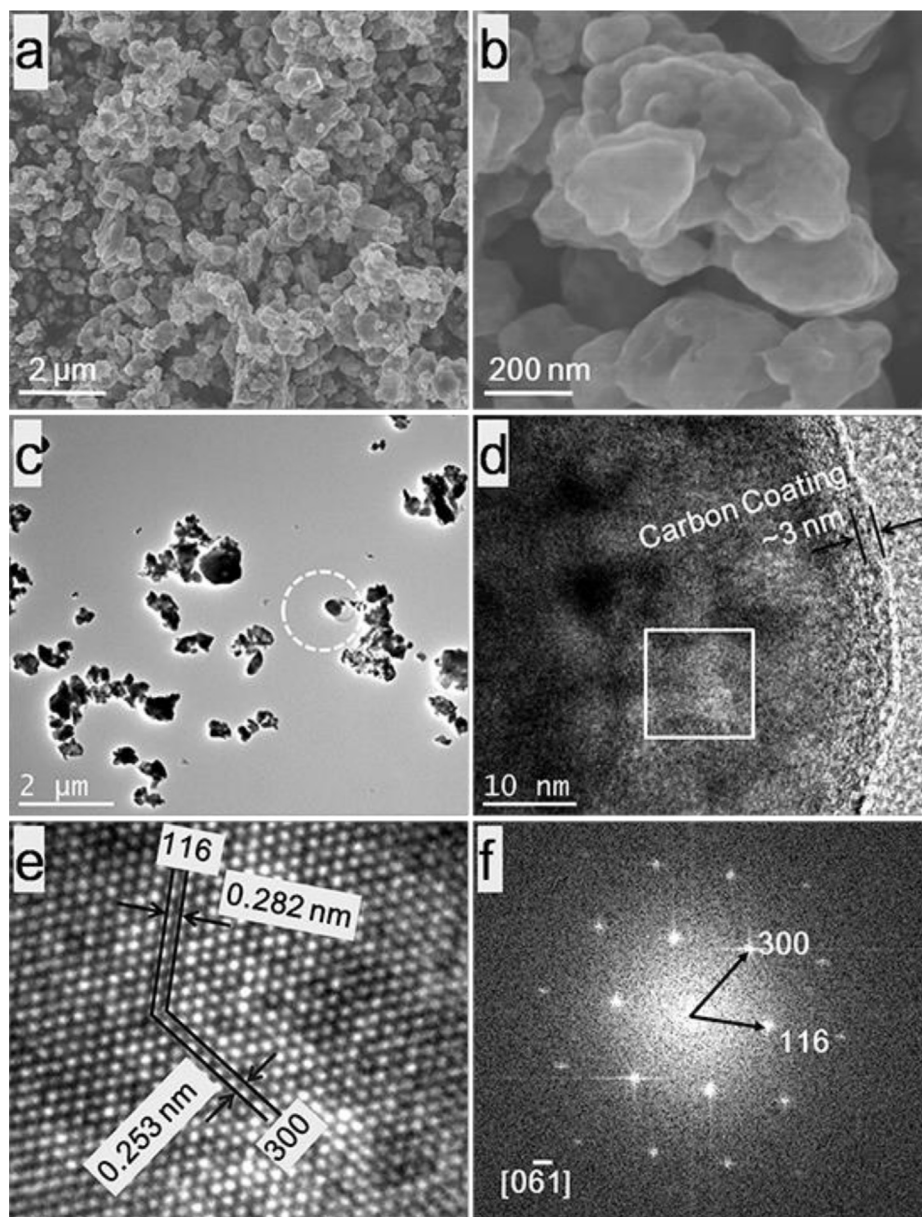


Fig. 3. (a) Low- and (b) high-magnification FESEM images of the NVP/C composite synthesised by carbon-thermal reduction at 900 °C. HRTEM images of the composite under (c) low magnification and (d and e) high magnification. (f) The corresponding SAED pattern.

Fig. 4(b) shows the CV curves of the electrode formed using the synthesised NVP/C composite synthesised at 900 °C for different scan rates; the potentials ranged from 2.7 to 4.0 V. The CV curves shown are related to only one redox couple, the one corresponding to the two compositional transitions between $\text{Na}_3\text{V}_2(\text{PO}_4)_3$ and $\text{NaV}_2(\text{PO}_4)_3$. As can be seen from the figure, there were a few obvious differences between the various CV curves. As the scan rate was increased, the cathodic and anodic peaks moved to lower and higher potentials, respectively, and the peak intensity increased. The difference in the potential of the anodic peaks and that of their corresponding cathodic peaks became larger with the increase in the scan rate. This was further evidence of the irreversible nature of the electrochemical reactions, owing to the degree of electrode polarisation being higher at the higher scan rates. Because the extraction/insertion of Na^+ ions into the NVP particles is a diffusion process, the electrode reaction can be attributed to semi-infinite and finite diffusion. The peak current in the case of the diffusion-

controlled behaviour is proportional to the square root of the scan rate. This relation can be expressed by the classical Randles–Sevcik equation [47,48]:

$$I_p = 2.69 \times 10^5 n^{3/2} S D_{\text{Na}}^{1/2} \nu^{1/2} C_0 \quad (1)$$

where I_p is the peak current (A), n is the number of electrons transferred per molecule during the electrochemical reaction, S is the active surface area of the electrode (cm^2), C_0 is the concentration of Na^+ ions in the bulk of the electrode (mol cm^{-3}), D_{Na} is the apparent diffusion coefficient of Na ions in the solid state ($\text{cm}^2 \text{s}^{-1}$), and ν is the potential scanning rate (V s^{-1}). On the basis of Eq. (1), the value of D_{Na} can be calculated from the slopes of the I_p vs. $\nu^{1/2}$ curves. Fig. 4(c) shows the relation between the anodic/cathodic peak currents (I_p) and the square root of the scan rates ($\nu^{1/2}$), confirming that the behaviour was diffusion controlled. The calculated values of D_{Na} were 3.57×10^{-13} and $5.81 \times 10^{-12} \text{ cm}^2 \text{s}^{-1}$

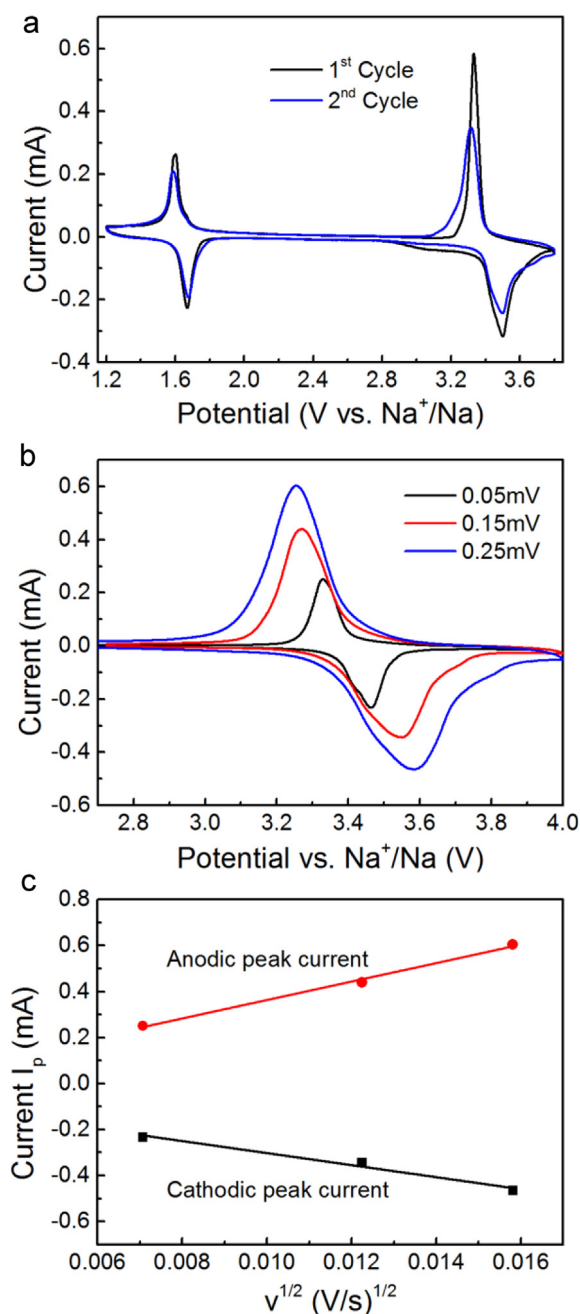


Fig. 4. (a) CV curves of the NVP/C composite synthesised at 900 °C at a scan rate of 0.05 mV s⁻¹ for potentials ranging from 1.2 to 3.8 V (vs. Na⁺/Na), (b) CV curves of the composite obtained at scan rates of 0.05, 0.15, and 0.25 mV s⁻¹, and (c) anodic/cathodic peak currents (*I_p*) as functions of the square root of the scan rates (*v*^{1/2}).

according to cathodic and anodic peak current, respectively. These values were 2–3 orders of magnitude larger than that of Li ions in Li₃V₂(PO₄)₃/C, as Na has a larger ionic radius.

The electrochemical properties of the Na half-cells fabricated using the synthesised composites as the cathode material are shown in Fig. 5. Fig. 5(a) shows the initial charge–discharge voltage profiles of the cathodes based on the NVP/C composites synthesised at different temperatures; the current rate was 0.1C and the potentials ranged from 2.5 to 3.8 V (vs. Na⁺/Na). The curves indicate that two Na⁺ ions were extracted from/inserted into NVP per formula unit during the charging/discharging processes, which lasted for 10 h. As can be seen from the figure, the charge curves for

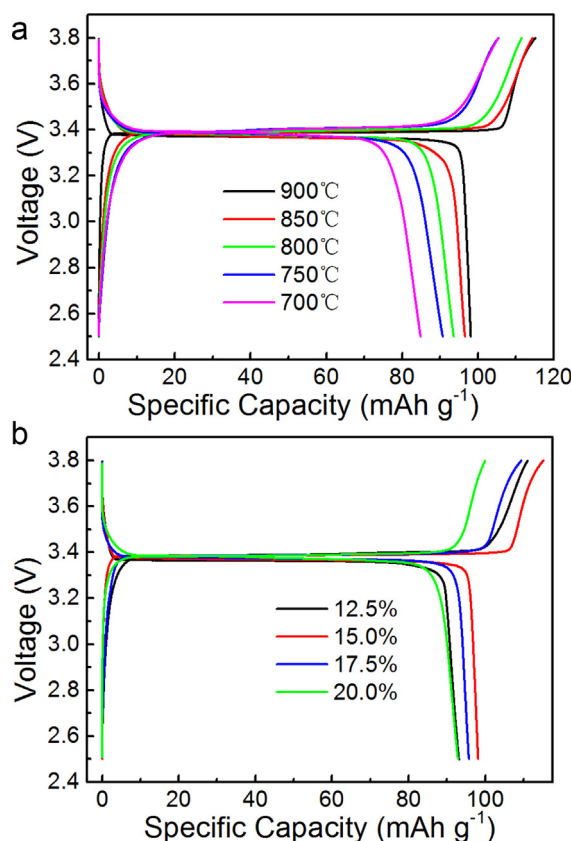


Fig. 5. (a) Initial charge–discharge curves of the samples synthesised at various temperatures for potentials ranging from 2.5 to 3.8 V. (b) Initial charge–discharge curves of the NVP/C samples with various glucose contents at the current rate of 0.1C; the potentials ranged from 2.5 to 3.8 V.

all the cathodes exhibited a plateau at approximately 3.4 V and so did the corresponding discharge curves; these were attributable to the two-phase transitions that occur during the electrochemical reaction and agreed well with the CV curves showed in Fig. 4(a). The sample synthesised at 900 °C exhibited the longest charge–discharge plateaus and the smallest difference in the potentials associated with the charge and discharge plateaus. This indicated that this cathode had the lowest degree of electrochemical polarisation and thus exhibited the highest reversibility with regard to the charging/discharging processes; this observation can be attributed to the higher crystallinity and uniform, sub-micron particle size of the sample. It can be seen from Fig. 5(a) that the initial discharge capacities for the NVP/C composite samples synthesised at 700, 750, 800, 850, and 900 °C, when measured over a period of 4 h at potentials ranging from 2.5 to 3.8 V, were 84.88, 90.72, 93.62, 96.61, and 98.17 mAh g⁻¹, respectively. It should be noted that the initial charge capacity of the sample synthesised at 900 °C was 115.18 mAh g⁻¹, which is very close to the theoretical capacity (117.6 mAh g⁻¹) of NVP for this range of potentials. The initial coulombic efficiency of the samples was approximately 85%, which is close to the value reported by other research groups [43]. The discharge capacity of the sample synthesised at 900 °C decreased slowly, from 98.17 mAh g⁻¹ during the 1st cycle to 93.35 mAh g⁻¹ during 50th cycle, indicating that it retained 95.08% of its initial discharge capacity. This again indicated high electrochemical reversibility. On the other hand, the sample synthesised at 700 °C retained 91.35% of its initial capacity after 50 cycles. Thus, the discharge capacity retention rate decreased gradually with a decrease in the annealing temperature, demonstrating that the

synthesis temperature has a significant effect on the electrochemical cycling performance. The fact that the potential profiles of the different samples during the cycling process were similar indicates that the extraction/insertion of Na ions does not cause significant changes to the material structure; this is because the volumetric change during the two-phase transition between $\text{Na}_3\text{V}_2(\text{PO}_4)_3$ and $\text{NaV}_2(\text{PO}_4)_3$ is small.

It is known that Na occupies two different positions in the NVP structure. Therefore, on the basis of the extraction of three Na^+ ions from the NVP lattice, the theoretical capacity of NVP can be said to be 176 mAh g^{-1} . However, the extraction of the third Na^+ ion is kinetically difficult, owing to the significantly lower electronic conductivity of the end-member of $\text{V}_2(\text{PO}_4)_3$ [44] and the lower Na-occupancy energy of the M1 sites [42]. Therefore, the two Na ions located at the M2 sites can be extracted/inserted easily and reversibly between 2.5 and 3.8 V on the basis of the $\text{V}^{3+}/\text{V}^{4+}$ redox couple, giving rise to the theoretical capacity of 117.6 mAh g^{-1} . That phosphate-based Na-insertion hosts are preferable can be attributable to the strong inductive effect of the covalent $(\text{PO}_4)_3^{2-}$ units. These units moderate the energetics of the transition metal redox couple and result in the operating potentials of these compounds (i.e., phosphate-based Na-insertion hosts) being relatively high. In addition, the compounds exhibit high thermal safety and structural stability even at high temperature states, in contrast to oxide-based Na-insertion hosts, as reported in previous literature [42]. Moreover, the presence of the thin carbon layer on the particle surfaces restrains particle growth at high temperatures and results in the formation of a conductive network, which improves electronic conductivity significantly. As a result, the obtained NVP/C composite exhibited significantly improved electrochemical performances in NIBs even at high charge–discharge rates.

Because the carbon shell layer improves the discharge capacity and the rate cycling performance of the NVP/C composite (pure NVP exhibits poor electrical conductivity), the amount in which glucose is added had a significant effect on the charge–discharge capacity and electrochemical reversibility of the resulting composite. Fig. 5(b) shows the initial charge–discharge curves of NVP/C samples having different thicknesses of the carbon shell layer owing to different glucose contents; the charge rate was 0.1C and the potentials ranged from 2.5 to 3.8 V. As can be seen from the figure, the voltage interval decreased with an increase in the glucose content. For instance, in the case of the sample with 12.5 wt % glucose, the sloping voltage plateaus and the large difference between the voltages corresponding to its charge and discharge plateaus were representative of its relatively high polarisation and sluggish kinetics; these, in turn, can be attributed to its poor electronic conductivity owing to the low thickness of the carbon shell layer. The initial discharge capacities of the samples with glucose contents of 12.5%, 15%, 17.5%, and 20% were 93.16, 98.12, 95.74, and 92.90 mAh g^{-1} , respectively. It should be noted that the discharge capacity of the sample with a glucose content of 12.5% was lower than that of the sample with a glucose content of 15%, indicating that a thin carbon shell layer had a negative effect on the specific discharge capacity of the composite, as this led to its electrical conductivity being low. However, it is important to point out that the discharge capacities decreased with the increase in the thickness of carbon shell layer owing to the increase in the glucose content when the thickness of carbon shell layer was enough, particularly for the samples with the glucose contents of 17.5% and 20.0%. The coulombic efficiency increased with the increase in the glucose content, indicating that there was a significant increase in the electrical conductivity with an increase in the thickness of the carbon layer. After the 50th cycle, the rates of discharge capacity retention of the composites with glucose contents of 12.5%, 15%, 17.5%, and 20% were 93.5%, 95.1%, 95.6%, and 96.4%, respectively,

showing an increase with the increase in the carbon content. That the coulombic efficiency and cycling performance increased significantly with the increase in the glucose content can be attributed to the resulting improvement in electrical conductivity. On the other hand, the calculated specific capacity values suggested that the discharge capacity of the composite decreased slightly when the residual carbon coating layer was too thick. Therefore, the amount of glucose used during synthesis is one of the most important factors determining the electrochemical performance of the NVP/C composite.

Fig. 6(a) shows the initial charge–discharge curves of the sample synthesised at 900°C at various C rates; the potentials ranged from 2.5 to 3.8 V (vs. Na^+/Na). It can be observed that the initial discharge capacities for the sample at the current rates of 0.1, 0.2, 0.5, 1, 2, 5, 10, 20, and 30C were 98.17, 97.62, 96.52, 95.26, 93.66, 91.63, 88.21, 84.90, and 76.44 mAh g^{-1} , respectively. Surprisingly, the electrode exhibited satisfactory performance even at 20 and 30C; the initial discharge capacities at these rates were much higher than those reported in the literature. This indicates that the electrode continued to exhibit excellent rate performance and retained 77.86% of its initial specific capacity during discharge when the current rate was increased from 0.1C to 30C. Fig. 6(b) shows the cycling performance of the NVP/C electrode at various C rates. Between the voltages of 2.5–3.8 V, the electrode exhibited good cyclability within the first 50 cycles; the losses in the discharge capacity between the 1st and the 50th cycles were less than 7.9% and 13.4% at 1C and 10C, respectively. When cycled at a current rate of 30C, the electrode retained a reversible capacity of 58.79 mAh g^{-1} throughout the 50 cycles, indicating that, in this material, the insertion/extraction of Na ions was highly repeatable

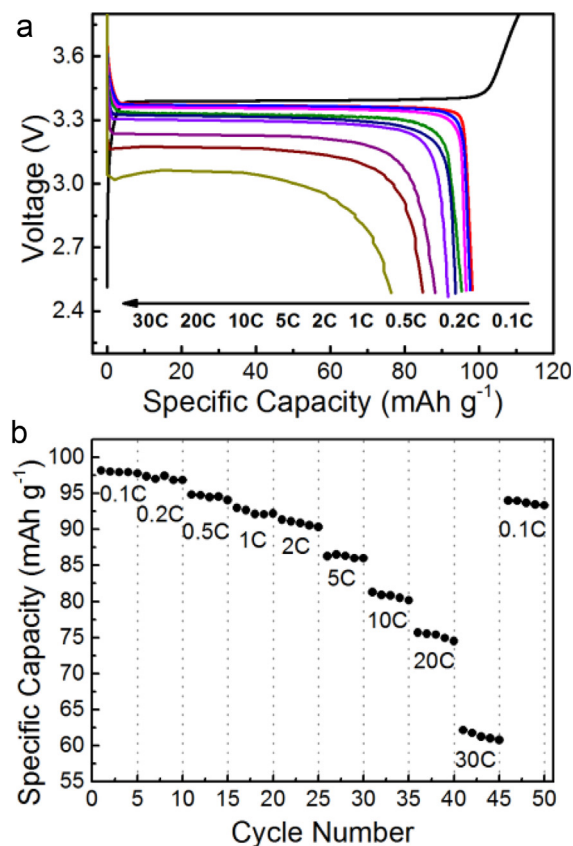


Fig. 6. (a) Initial charge–discharge curves and (b) cycling performances of the samples at various C rates; the potentials ranged from 2.5 to 3.8 V.

even at high current rates. The high cyclability was indicative of a stable crystal framework within the NASICON-type structure. The high rate capacity and excellent cyclability of the NASICON-type cathode can be attributed to the small size of the NVP/C crystals, their narrow size distribution, and the sufficiently thick carbon coating that formed *in situ* on the surfaces of its particles. This coating, which acts as an electrical conduit during the electrochemical reaction, appears to improve interparticle connectivity and thus the electronic conductivity. Furthermore, the high cyclability and rate performance can also be attributed to the well-defined 3D channel structure of the composite, which facilitates the insertion/extraction of Na^+ ions; this was in keeping with its NASICON-type structure.

It can be seen clearly from the CV curves (Fig. 4(a)) that NVP also exhibits a redox couple in the low-voltage region. Therefore, it could potentially be used as an anodic material for NIBs based on the $\text{V}^{2+}/\text{V}^{3+}$ redox couple, which corresponds to the two-phase transition between $\text{Na}_3\text{V}_2(\text{PO}_4)_3$ and $\text{Na}_4\text{V}_2(\text{PO}_4)_3$. It is known that one-third of the M2 sites in the crystal structure of NVP are not occupied, owing to the relatively unstable oxidation state of V^{2+} . On the other hand, when the electrode is discharged at voltages lower than 1.6 V, Na^+ ions can occupy all of these positions under an electric field. This is what results in the occurrence of the two-phase transition reaction at approximately 1.6 V. Fig. 7(a) shows the 1st cycle charge–discharge curves of the electrode based on the NVP/C composite synthesised at 900 °C for different current rates; the cut-off potentials ranged from 1.0 to 2.5 V. It can be seen clearly that all the charge–discharge curves exhibit a redox plateau at approximately 1.6 V. The initial discharge capacities of the electrode were 63.2, 62.53, 61.59, 60.16, 56.55, 51.65, 46.15, 42.49, and

36.74 mAh g^{-1} at current rates of 0.1, 0.2, 0.5, 1, 2, 5, 10, 20, and 30C, respectively. This indicates that the material had excellent rate performance and a discharge specific capacity retention rate of 58.1% even when the current rate was increased from 0.1C to 30C. Interestingly, in addition to the excellent properties displayed when used as a cathode, the NVP/C composite also exhibited a high rate capacity and excellent cyclability when used as an anode. The charge and discharge curves plateaued at approximately 1.71 V and 1.58 V (vs. Na^+/Na), respectively, at the current rate of 0.1C; this was in keeping with what was observed in the CV curves as well. During subsequent cycles, the observed voltage profiles remained unaltered, demonstrating that the composite had excellent reversibility during the cycling process. The initial reversible capacity was 63.2 mAh g^{-1} , and the discharge capacity remained at 60.29 mAh g^{-1} after 50 cycles, with discharge capacity retention rate being 95.4%. Fig. 7(b) shows the cycling performance of the synthesised material at different current rates. The discharge capacities were 56.13, 39.78, and 29.82 mAh g^{-1} after the 50th cycle for current rates of 1, 10, and 30C, respectively, with the discharge capacity retention rates being 93.3%, 86.2%, and 81.2%, respectively. It can be concluded that the cycling performance of the NVP/C composite was good. At the high current rates, the material exhibited stable cyclability, indicating that the insertion/extraction of Na^+ ions in the system does not affect its cyclability and that the crystal structure of the material remains relatively unchanged under the higher discharge current.

To further understand the electrode reaction kinetics of the composite, EIS measurements were performed before and after the 1st cycle for frequencies ranging from 0.01 Hz to 100 kHz during the discharge state. EIS is a useful technique for evaluating the diffusion coefficient of Na^+ ions and the changes in the impedance of the sample. This is because the Warburg impedance of an electrode material in the low-frequency range is directly related to the Na-ion diffusion process in the material [48]. Fig. 8(a) shows the Nyquist plots of the NVP/C composite synthesised at 900 °C. The plots were obtained under an open-circuit potential during the discharge stage; the equivalent circuit model is shown in the inset. It can be seen that the Nyquist plots consist of a small intercept in the high-frequency region, two partially overlapping curved sections in the high- and medium-frequency regions, and a linear part in the low-frequency region. The very small intercept on the Z_{real} -axis in the high-frequency region is attributable to the combined resistance (R_e) of the electrolyte, the separator, and the electrode. The curved sections in the high- and medium-frequency ranges are attributable to the charge-transfer impedance (R_{ct}) and the double-layer capacitance at the electrode–electrolyte interface (i.e., the solid-electrolyte interphase or SEI), while the sloping line in the low-frequency range corresponds to the Warburg impedance, which is associated with the diffusion of Na ions in the bulk of the electrode material [49]. It can be seen that the charge-transfer resistance after the 1st cycle was larger than that before the 1st cycle. This is mainly because the continuous deposition of Na ions in the SEI film increases its thickness, which, in turn, increases the charge-transfer resistance. The inset in Fig. 8(a) shows the equivalent circuit used to obtain the electrochemical impedance spectrum data. Here, R_e represents the solution resistance, and R_{ct} is the charge transfer resistance. Z_W represents the Warburg impedance, which is related to the solid-state diffusion of ions in the active material and corresponds to the sloping line in the low-frequency region. Q_{ct} is associated with the surface property of the electrode. C_{int} is the capacitance resulting from ion transfer in the active material [44]. The fitting parameters are shown in Table 5. All the errors were within bounds. It can be seen that the charge-transfer resistance at the electrolyte–electrode interface is one of the primary reasons for the poor performance of the electrode.

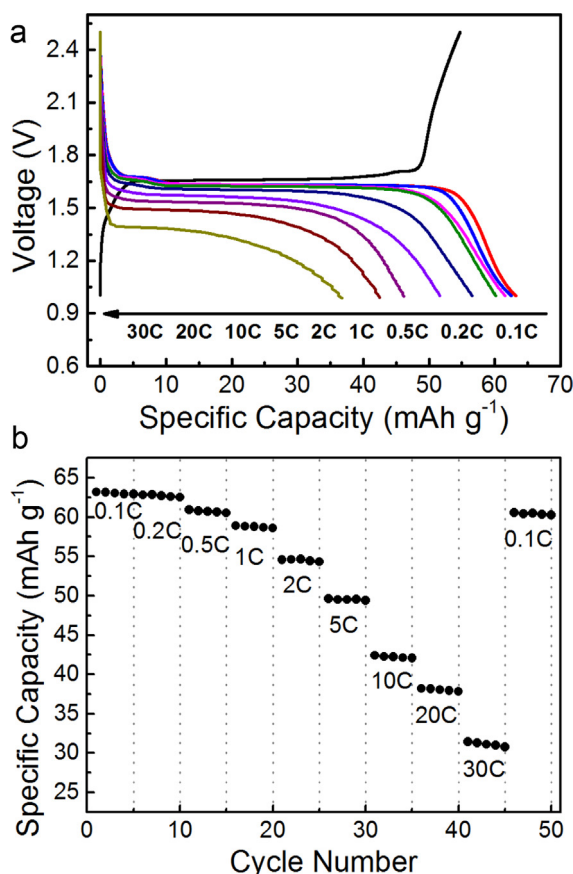


Fig. 7. (a) Initial charge–discharge curves and (b) cycling performances of the samples at various C rates; the potentials ranged from 1.0 to 2.5 V.

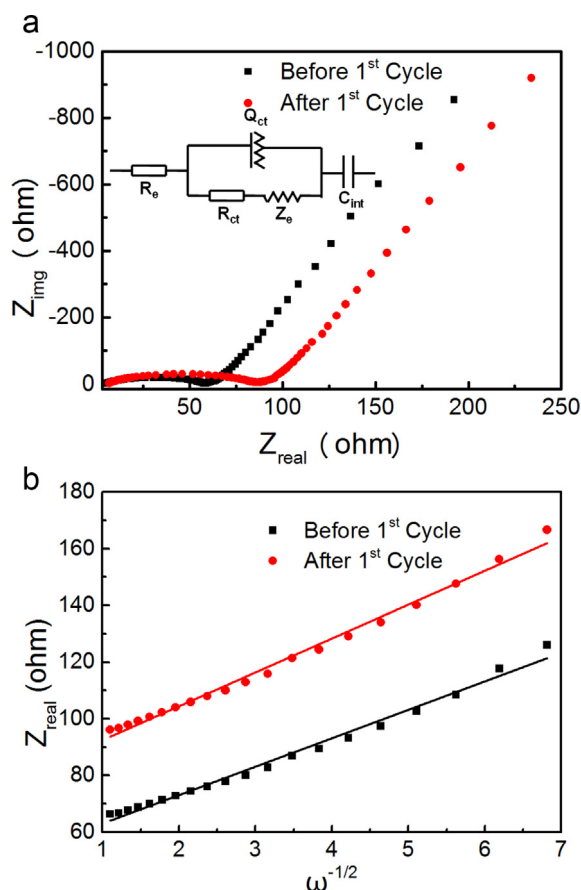


Fig. 8. (a) Nyquist plots of the NVP/C composite electrodes before and after the 1st cycle and (b) linear fits of the Z_{real} vs. $\omega^{-1/2}$ curves of the composite synthesised at 900 °C corresponding to the discharge state.

The apparent diffusion coefficient of the Na^+ ions (D_{Na}) can be estimated from the low-frequency regions of the plots using the following two equations [44,47]:

$$D_{\text{Na}} = \frac{1}{2} \left[\left(\frac{V_m}{FS\sigma} \right) \left(\frac{dE}{d\delta} \right) \right]^2 \quad (2)$$

$$D_{\text{Na}} = \frac{0.5R^2T^2}{S^2n^4F^4C^2\sigma^2} \quad (3)$$

It is obvious that Eq. (1) is not suitable in the present case, owing to the titration potential curve being flat [47]. In Eq. (2), R is the gas constant, T is the absolute temperature, S is the active surface area of the cathode, n is the number of electrons per species reaction during oxidation, F is the Faraday constant, C is the concentration of Na ions in the cathode electrode (which was approximately $6.92 \times 10^{-3} \text{ mol cm}^{-3}$, given the chemical composition of the active

material) [44], and σ is the Warburg factor, which obeys the following relationship [47]:

$$Z_{\text{real}} = R_e + R_{\text{ct}} + \sigma\omega^{-1/2} \quad (4)$$

where R_e is the resistance between the electrolyte and the electrode, and R_{ct} is the charge-transfer resistance.

Fig. 8(b) shows the linear relationship between Z_{real} and the square root of the frequency ($\omega^{-1/2}$) in the low-frequency region, from which the slope, σ , was 10.04 (before 1st cycle) and $11.95 \text{ S}^{-1} \text{ s}^{-1/2}$ (after 1st cycle) can be obtained. Using this value of σ , it was possible to calculate the D_{Na} value of the composite. Thus, on the basis of Eq. (2), the D_{Na} values were calculated to be 4.59×10^{-13} and $3.24 \times 10^{-13} \text{ cm}^2 \text{ s}^{-1}$, respectively. It can be seen that the D_{Na} value obtained using EIS was similar to that obtained from the CV measurements. In addition, the values of D_{Na} for NVP obtained in this study were much higher than that of olivine NaFePO_4 ($8.63 \times 10^{-17} \text{ cm}^2 \text{ s}^{-1}$) [50], indicating that NVP could be a promising cathodic material for high-power NIBs. The difference in the ion-diffusion coefficients of the two phosphate materials is attributable to the differences in their structural properties. In the case of olivine NaFePO_4 , Na^+ ions can only be transported along a 1D pathway, while the NASICON-type structure of NVP allows Na^+ ions to be transported reversibly in a 3D framework, resulting in faster diffusion.

4. Conclusions

An NVP/C composite was successfully synthesised as an electrode material for NIBs by a carbon-thermal reduction method using glucose as the carbon source. The carbon coating on the NVP particles not only retarded the growth of the particles, but also improved the electronic contact between them, resulting in high electronic conductivity. The well carbon-coated ($\sim 3 \text{ nm}$ in thickness) NVP sample, which had a uniform particle size distribution, exhibited voltage plateaus at 3.4 V and 1.63 V; these were probably attributable to the $\text{V}^{4+}/\text{V}^{3+}$ and $\text{V}^{3+}/\text{V}^{2+}$ redox couples in the material, which showed promise as a cathodic as well as an anodic material for NIBs. The NVP/C composite exhibited high specific capacity and excellent cycling performance. This suggests that the extraction/insertion of Na ions does not make the system unstable. At the current rate of 0.1C, the NVP/C composite exhibited initial discharge capacities of 98.2 and 63.2 mAh g^{-1} for potentials ranging from 2.5 to 3.8 V and 1.0 to 2.5 V, respectively. The values of the apparent diffusion coefficient of Na ions in the NVP/C composite, determined using CV and EIS, were approximately 3.24×10^{-13} and $5.81 \times 10^{-12} \text{ cm}^2 \text{ s}^{-1}$, respectively. These values are higher than those for other Na ions-based cathodic materials. This can be attributed to the NASICON-type structure of the NVP/C composite, which allows for fast ion diffusion. Therefore, the synthesised NVP/C composite can be considered a suitable cathodic material for high-performance, rechargeable NIBs.

Acknowledgements

This work was supported by grants from the National High Technology Research and Development Program of China (No. 2007AA03Z301), the National Natural Science Foundation of China (No. 61076040), and the Specialized Research Fund for the Doctoral Program of Higher Education of China (No. 2012011111006).

References

- [1] J.B. Goodenough, K.-S. Park, *J. Am. Chem. Soc.* 135 (2013) 1167–1176.
- [2] B. Kang, G. Ceder, *Nature* 458 (2009) 190–193.

Table 5

Impedance parameters obtained by fitting the experimental data using the equivalent circuit.

	R_e ($\Omega \text{ cm}^{-2}$)	R_{ct} ($\Omega \text{ cm}^{-2}$)	Z_w ($\text{S s}^{1/2} \text{ cm}^{-2}$)	Q_{ct} ($\text{S s}^n \text{ cm}^{-2}$)	C_{int} (F cm^{-2})
Before 1st cycle	4.702	52.08	3.206E^{-2}	1.042E^{-5}	1.98E^{-2}
After 1st cycle	5.727	78.42	2.553E^{-2}	8.518E^{-6}	1.849E^{-2}

- [3] L. Zhang, H. Xiang, Z. Li, H. Wang, *J. Power Sources* 203 (2012) 121–125.
- [4] L. Dimesso, C. Förster, W. Jaegermann, J. Khanderi, H. Tempel, A. Popp, J. Engstler, J. Schneider, A. Sarapulova, D. Mikhailova, *Chem. Soc. Rev.* 41 (2012) 5068–5080.
- [5] M. Hu, X. Pang, Z. Zhou, *J. Power Sources* 237 (2013) 229–242.
- [6] Y. Wang, H. Zou, E. Gratz, D. Apelian, *Green Chem.* 15 (2013) 1183–1191.
- [7] H. Pan, Y.-S. Hu, L. Chen, *Energy Environ. Sci.* 6 (2013) 2338–2360.
- [8] K. Saravanan, C.W. Mason, A. Rudola, K.H. Wong, P. Balaya, *Adv. Energy Mater.* 3 (2012) 444–450.
- [9] J. Qian, X. Wu, Y. Cao, X. Ai, H. Yang, *Angew. Chem.* 125 (2013) 4731–4734.
- [10] P. Serras, V. Palomares, A. Goñi, P. Kubiak, T. Rojo, *J. Power Sources* 241 (2013) 56–60.
- [11] R. Shakoob, D.-H. Seo, H. Kim, Y.-U. Park, J. Kim, S.-W. Kim, H. Gwon, S. Lee, K. Kang, *J. Mater. Chem.* 22 (2012) 20535–20541.
- [12] H. Wang, W. Wang, Y. Ren, K. Huang, S. Liu, *J. Power Sources* 199 (2012) 263–269.
- [13] H. Liu, H. Zhou, L. Chen, Z. Tang, W. Yang, *J. Power Sources* 196 (2011) 814–819.
- [14] O. Szajwaj, E. Gaudin, F. Weill, J. Darriet, C. Delmas, *Inorg. Chem.* 48 (2009) 9147–9154.
- [15] D. Hamani, M. Ati, J.-M. Tarascon, P. Rozier, *Electrochem. Commun.* 13 (2011) 938–941.
- [16] M. Guignard, C. Didier, J. Darriet, P. Bordet, E. Elkaïm, C. Delmas, *Nat. Mater.* 12 (2012) 74–80.
- [17] C. Didier, M. Guignard, J. Darriet, C. Delmas, *Inorg. Chem.* 51 (2012) 11007–11016.
- [18] M. D'Arienzo, R. Ruffo, R. Scotti, F. Morazzoni, C.M. Mari, S. Polizzi, *Phys. Chem. Chem. Phys.* 14 (2012) 5945–5952.
- [19] H. Kim, D.J. Kim, D.-H. Seo, M.S. Yeom, K. Kang, D.K. Kim, Y. Jung, *Chem. Mater.* 24 (2012) 1205–1211.
- [20] E. Hosono, T. Saito, J. Hoshino, M. Okubo, Y. Saito, D. Nishio-Hamane, T. Kudo, H. Zhou, *J. Power Sources* 217 (2012) 43–46.
- [21] D.H. Lee, J. Xu, Y.S. Meng, *Phys. Chem. Chem. Phys.* 15 (2013) 3304–3312.
- [22] D. Kim, E. Lee, M. Slater, W. Lu, S. Rood, C.S. Johnson, *Electrochem. Commun.* 18 (2012) 66–69.
- [23] L. Vijayan, R. Cheruku, G. Govindaraj, S. Rajagopan, *Mater. Chem. Phys.* 125 (2011) 184–190.
- [24] P. Barpanda, Y. Tian, M. Avdeev, S.-C. Chung, A. Yamada, *J. Mater. Chem. A* 1 (2013) 4194–4197.
- [25] P. Barpanda, J. Lu, T. Ye, M. Kajiyama, S.-C. Chung, N. Yabuuchi, S. Komaba, A. Yamada, *RSC Adv.* 3 (2013) 3857–3860.
- [26] P. Barpanda, M. Avdeev, C.D. Ling, J. Lu, A. Yamada, *Inorg. Chem.* 52 (2013) 395–401.
- [27] M. Nose, H. Nakayama, K. Nobuhara, H. Yamaguchi, S. Nakanishi, H. Iba, *J. Power Sources* 234 (2013) 175–179.
- [28] Y. Zheng, P. Zhang, S. Wu, Y. Wen, Z. Zhu, Y. Yang, *J. Electrochem. Soc.* 160 (2013) A927–A932.
- [29] A. Langrock, Y. Xu, Y. Liu, S. Ehrman, A. Manivannan, C. Wang, *J. Power Sources* 223 (2012) 62–67.
- [30] K. Chihara, A. Kitajou, I.D. Gocheva, S. Okada, J.-I. Yamaki, *J. Power Sources* 227 (2012) 80–85.
- [31] T. Jiang, G. Chen, A. Li, C. Wang, Y. Wei, *J. Alloys Compd.* 478 (2009) 604–607.
- [32] W. Wang, C. Yu, Y. Liu, J. Hou, H. Zhu, S. Jiao, *RSC Adv.* 3 (2013) 1041–1044.
- [33] W. Wang, C. Yu, Z. Lin, J. Hou, H. Zhu, S. Jiao, *Nanoscale* 5 (2013) 594–599.
- [34] P. Senguttuvan, G.I. Rousse, V. Seznec, J.-M. Tarascon, M.R. Palacin, *Chem. Mater.* 23 (2011) 4109–4111.
- [35] A. Rudola, K. Saravanan, C.W. Mason, P. Balaya, *J. Mater. Chem. A* 1 (2013) 2653–2662.
- [36] Y. Sun, L. Zhao, H. Pan, X. Lu, L. Gu, Y.-S. Hu, H. Li, M. Armand, Y. Ikuhara, L. Chen, *Nat. Commun.* 4 (2013) 1870.
- [37] L. Zhao, J. Zhao, Y.S. Hu, H. Li, Z. Zhou, M. Armand, L. Chen, *Adv. Energy Mater.* 2 (2012) 962–965.
- [38] H. Zhou, M.-A. Einarsrud, F. Vullum-Bruer, *J. Power Sources* 235 (2013) 234–242.
- [39] J. Son, S. Kim, M. Kim, K. Kim, V. Aravindan, W. Cho, Y. Lee, *J. Appl. Electrochem.* 43 (2013) 1–11.
- [40] Y. Lu, L. Wang, J. Song, D. Zhang, M. Xu, J.B. Goodenough, *J. Mater. Chem. A* 1 (2013) 68–72.
- [41] Z. Jian, L. Zhao, H. Pan, Y.-S. Hu, H. Li, W. Chen, L. Chen, *Electrochem. Commun.* 14 (2012) 86–89.
- [42] S.Y. Lim, H. Kim, R. Shakoob, Y. Jung, J.W. Choi, *J. Electrochem. Soc.* 159 (2012) A1393–A1397.
- [43] Y.H. Jung, C.H. Lim, *J. Mater. Chem. A* 1 (2013) 11350–11354.
- [44] K. Du, H. Guo, G. Hu, Z. Peng, Y. Cao, *J. Power Sources* 223 (2013) 284–288.
- [45] I.V. Zatonovskiy, *Acta Crystallogr. E Struct. Rep. Online* 66 (2010) i12–i12.
- [46] J. Kang, S. Baek, V. Mathew, J. Gim, J. Song, H. Park, E. Chae, A.K. Rai, J. Kim, *J. Mater. Chem.* 22 (2012) 20857–20860.
- [47] T. Jiang, W. Pan, J. Wang, X. Bie, F. Du, Y. Wei, C. Wang, G. Chen, *Electrochim. Acta* 55 (2010) 3864–3869.
- [48] Y. Qiao, X. Wang, J. Xiang, D. Zhang, W. Liu, J. Tu, *Electrochim. Acta* 56 (2011) 2269–2275.
- [49] J. Su, X.-L. Wu, J.-S. Lee, J. Kim, Y.-G. Guo, *J. Mater. Chem. A* 1 (2013) 2508–2514.
- [50] Y. Zhu, Y. Xu, Y. Liu, C. Luo, C. Wang, *Nanoscale* 5 (2013) 780–787.